Universiteit
Leiden
The Netherlands

Surface plasmon lasers

Tenner, V.T.

Citation
Tenner, V. T. (2017, June 22). *Surface plasmon lasers*. *Casimir PhD Series*. Retrieved from https://hdl.handle.net/1887/49932

Version:	Not Applicable (or Unknown)
License:	Licence agreement concerning inclusion of doctoral thesis in the Institutional Repository of the University of Leiden
Downloaded from:	https://hdl.handle.net/1887/49932

Note: To cite this publication please use the final published version (if applicable).

Cover Page

Universiteit Leiden

The handle http://hdl.handle.net/1887/49932 holds various files of this Leiden University dissertation.

Author: Tenner, V.T.
Title: Surface plasmon lasers
Issue Date: 2017-06-22

Chapter 3

Loss and scattering of surface plasmon polaritons on optically pumped hole arrays

We study surface plasmons on 2-dimensional square arrays of sub-wavelength holes in a gold film deposited on an optically-excited semiconductor. We observe four resonances of which we measure the resonance frequencies, the spectral widths, and the relative intensities. The spectral widths allow us to quantify various loss processes, including ohmic loss, optical absorption/gain and radiative scattering loss. Prominent kinks in the plasmon dispersion relation occur around the Rayleigh anomaly. A coupled mode model that includes a frequency dependent gain of the semiconductor reproduces the main features in the experimental data.

This chapter was previously published as:
V. T. Tenner, A. N. van Delft, M. J. A. de Dood, and M. P. van Exter, *Loss and scattering of surface plasmon polaritons on optically-pumped hole arrays*, Journal of Optics **16**, 114019 (2014)

3.1 Introduction

Surface plasmons polaritons or surface plasmons (SPs) are a combined optical and electronic solution to Maxwell equations bound to an interface. These surface plasmons can be localized on a nano particle, or they can be traveling along an extended interface. One remarkable property of SPs is the strong confinement normal to the interface, with exponentially decaying fields in both media. Several applications benefit from the strong confinement of the field that can be used to enhance the light-matter interaction, for example in molecular sensors [53, 54]. The strong confinement can also be used to guide SP and build plasmonic circuits, including beam splitters [55]and phase manipulators [56]. Similarly, meta-materials often consist of sub-wavelength metal structures where the plasmon modes are responsible for many of their extraordinary properties, such as the ability to create negative refractive index materials [7, 8].

Although SP-based systems are highly succesfull, the main limiting factor is loss, which can be divided in (ohmic) absorption loss and scattering loss. For instance, SPs traveling on smooth Ag or Au interfaces are typically absorbed after 2-100 μm [57] for wavelengths between 0.5 and 1.5 μm. Gain can be introduced to overcome this limitation and several demonstrations of complete loss compensation have been shown, using a semiconductor [19] or dye [40] as gain material. SP-lasing action is possible when complete loss compensation is combined with a mechanism for optical feedback. This feedback has been demonstrated in several structures [58], including metal-coated nano-pillars [22], gold nano-spheres [21], and metal hole arrays [20].

In this chapter, we study the modes of metal hole arrays with gain. These structures are comparable to the structures that we have studied before [20, 37]. To gain insight in the lasing mechanism it is essential to identify the modes responsible for lasing. This can be done by measuring the dispersion of plasmonic bands and quantifying the spectral width of these modes. This analysis is best performed below the lasing threshold, where optical saturation and other nonlinear optical processes are not yet relevant. In our earlier work we reported avoided crossings of the mode frequencies and compared this to a coupled mode model [37]. In this chapter, we extend this analysis and extract the frequency, width and total intensity of each mode, by fitting the angle dependent emission spectra. The measured width allows to quantify the effective ohmic loss as well as the scattering loss rate. We augment the coupled mode model to include frequency dependent gain. This extended coupled mode model captures all the main features without introducing a large number of unknown parameters. This allows to identify the physical mechanisms that are most relevant to lasing action of SPs in metal hole arrays. This simplified model necessarily misses some of the details that are visible in the experimental data. Most notably, we identify abrupt changes in the dispersion of the plasmonic bands and the associated width of the resonances that coincide with a Rayleigh anomaly.

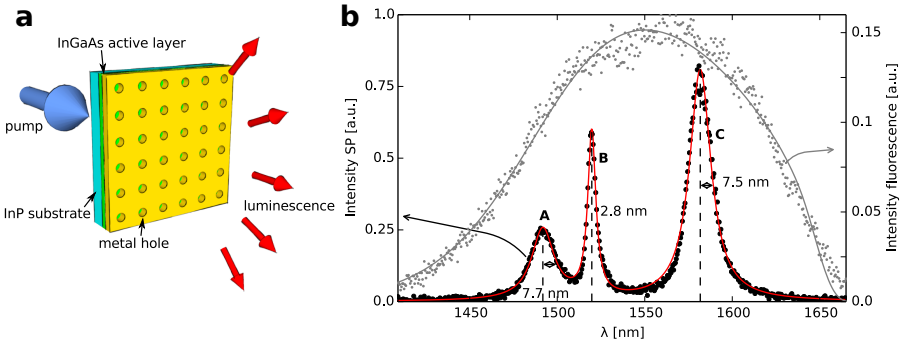

Figure 3.1: a) Sketch of setup. Samples are optically pumped through the substrate and fluorescence is collected through the hole array. A fiber on a translation stage placed in the far field allows to measure spectra as a function of angle. b) Spectrum of p-polarized light emitted at ($\theta_x = 0$, $\theta_y = 0.10$) rad. The fit (red curve) is based on a sum of three Lorentzian resonances. The half widths of these peaks are indicated in the graph. The grey symbols show the measured fluorescence on a piece of the wafer without a gold layer. The line through this data is a model that describes the frequency dependent gain (see text).

3.2 Methods

3.2.1 Sample

The semiconductor-gold samples that we studied are identical to the ones described in refs [20, 37]. Their layer structure, depicted in Fig. 3.2, comprise a 100 nm thick gold film on a 105 nm thick $In_xGa_{1-x}As$ semiconductor layer that is lattice matched ($x \simeq 0.53$) to a 300 μm thick, double polished, InP substrate. A 15-20 nm thick SiN_x/InP spacer-layer between the $In_xGa_{1-x}As$ and the gold prevents quenching of the optically excited semiconductor. A 20 nm thick chromium layer on top of the gold damps the SP resonance on the gold-air interface, leaving only the gold-semiconductor resonances. The gold layer is perforated with holes with a diameter of 180 nm. The holes are arranged in a 50x50 μm square grid with a spacing $a_0 = 470$ nm between the holes.

3.2.2 Experimental geometry

Fig. 3.1a shows the experimental geometry. We optically excite the InGaAs active/gain layer through the InP substrate with a continuous-wave pump laser with a wavelength of 1064 nm. The resonances of the system are all visible below the laser threshold, and hence the incident power (120 mW) was kept below laser threshold of the device at a temperature of 120 K. The pump spot on the sample had

a square shape with a size of 45x45 μm^2. This pump beam creates electron-hole pairs in the active layer of InGaAs material. These carriers radiatively recombine and couple light into the plasmon modes of the metal hole array living on the gold-semiconductor interface. The grey curve in Fig. 3.1b shows the measured spectrum of this radiative recombination for a part of the sample without gold.

The collection part of our setup was the same as in [20, 37]. The fluorescence light was collected in the far field at the gold side of the sample as a function of angle (θ_x, θ_y). More precisely, the light was collected using a 20x microscope objective with a numerical aperture of 0.4. Sequentially the array structure was magnified 20x by a lens with a 20 cm focal length. Finally, the far field of the sample was reached in the back-focal plane of a lens (focal length 5 cm), where the fluorescence light was collected on a spectrometer using a single mode optical fiber ($w \approx 10\mu m$ $@\lambda = 1500$ nm). This fiber was scanned in the far field by a 2-dimensional translation stage. In this chapter we keep the fiber at $\theta_x = 0$ and scan the fiber only in the θ_y direction, from $\theta_y = -0.44$ rad to $\theta_y = 0.44$ rad in 110 steps, but we limit all figures to the most relevant part $-0.3 \leq \theta_y \leq 0.3$. The angle θ_y is related to the in-plane momenta in the y-direction (Γ-M) by $k_{\|} = (\omega/c) \sin\theta_y$[37]. A thin film polarizer was used to discriminate between vertical (p=TM) and horizontal (s=TE) polarized light.

Figure 3.1b shows a typical p-polarized emission spectrum, obtained at an angle $\theta_y = 0.10$. This spectrum contains three peaks, labeled by A, B and C. A curve consisting of three Lorentzians fits the data very well. We repeated these measurements at other angles θ_y and for both polarizations, where similar high quality fits yielded the position, the spectral width (half height half maximum, HWHM), and the integrated intensity of each of the three peaks. The observed angle dependence of the frequencies, spectral widths, and integrated intensities of these resonances are discussed below.

3.3 Theory

We analyze all our data with a model based on four coupled surface plasmon modes. This model, which is discussed in the Appendix, extends the work of [37]. It includes the SP-to-SP scattering that dominantly determines the SP dispersion relation [37]. As an extension it also includes SP losses due to SP-to-photon scattering, ohmic losses, and optical gain. These loss/gain channels determine the spectral widths of the resonances. We describe these losses as imaginary rates in the coupled mode model and thus obtain a complex plasmonic bandstructure.

Our model contains the following parameters: SP-to-SP coupling is parameterized by scattering rates γ and κ, which refer to back-scattering and right-angle-scattering, respectively[37]. The ohmic loss and optical gain are combined into a reduced ohmic loss rate $\Gamma_R = \Gamma_r - g(\omega)$, where the ohmic loss Γ_r rate includes surface-roughness related effects. Finally, SP-to-photon coupling occurs at a radiative loss rate Γ_{rad} for the traveling waves, and at loss rates $2\Gamma_{\text{rad}}$ or 0 for the standing

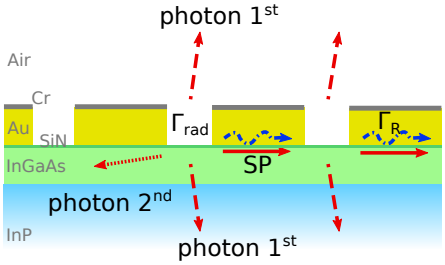

Figure 3.2: Loss channels of SP. The reduced ohmic loss, denoted by the loss rate Γ_R, is spatial uniform and includes the effective optical gain. The radiative loss, denoted by the loss rate Γ_{rad}, occurs only at the holes and originates from scattering of SPs to photons. At large angle, the SP-to-photon scattering is distributed over three diffraction orders: 1st order diffraction into the air, and 1st and 2nd order diffraction into the semiconductor. We only observe the emission into air and analyze it as a function of frequency and emission angle.

waves (depending on the positions of their nodes).

The various loss channels are depicted in Fig. 3.2. The radiative loss originates from scattering of surface plasmons to photons in air and to photons in the semiconductor. At sufficiently large angles a Rayleigh anomaly becomes visible in the data. This anomaly opens a second scattering channel and is expected to lead to an increase in the radiative loss [59] and may affect the SP dispersion via a Kramer-Krönig-type relation. This second scattering channel is denoted as photon 2nd in Fig. 3.2, where the other channels are denoted as photon 1st.

By combining the (complex) amplitudes of the four coupled SP modes in a four-vector $|E(t)\rangle$, the time evolution of the SP field can be described by a single equation

$$\frac{d}{dt}|E(t)\rangle = -iH|E(t)\rangle + |S(t)\rangle\,, \tag{3.3.1}$$

where the evolution matrix H contains all scattering and loss/gain processes. The vector $|S(t)\rangle$ describes the spontaneous emission that continuously feeds the SP field (see Appendix for details). We use two versions of this equation to model our experimental results. In our basic model we keep all parameters in the evolution matrix constant and neglect the frequency dependence of the spontaneous emission. This model is most easy to implement and already demonstrates various key features of the system, such as the separation of the four coupled modes into three p-polarized modes and one s-polarized mode. The symmetry of the square lattice also force the modes to be radiative and non-radiative modes. In our advanced model we include the most prominent frequency dependences, being that of the spontaneous emission $S(\omega)$ and the optical gain $g(\omega)$. For simplicity, and to keep the number of fit parameters limited, we will not include the milder frequency dependences of

the various scattering rates and the appearance of the additional scattering channel depicted in Fig. 3.2.

The spontaneous and stimulated emission in the semiconductor originate from radiative recombination of electron-hole pairs. These emission rate, and the associated optical gain, depends on the density of states of electrons and holes in the conduction and valence bands and their fractional occupations $0 < f_{c/v} < 1$. For the usual parabolic bands, the electronic density of states has a $\sqrt{E - E_g}$ dependence above the bandgap E_g, while the fractional occupations are Fermi-Dirac functions of the form $f_{c/v} = 1/[1 + \exp(E - E_{F,c/v})/k_B T]$. The optical transitions are direct, i.e. $\Delta k \approx 0$, and the heavy hole mass of lattice-matched InGaAs is much larger than the effective electron mass ($m_h/m_e \approx 5$) [60]. As a result, the frequency dependence of the emission rate is well approximated by the occupation in the conduction band. We model the emission rate and frequency dependent gain as [61]

$$\begin{aligned} S(\omega) &\propto \sqrt{\hbar\omega - E_g} f_c (1 - f_v) \\ &\approx \sqrt{\hbar\omega - E_g} \frac{1}{1 + \exp(\hbar\omega - E_{F,c})/k_B T} (1 - f_{v,0}), \end{aligned} \tag{3.3.2}$$

$$\begin{aligned} g(\omega) &\propto \sqrt{\hbar\omega - E_g} (f_c - f_v) \\ &\approx \sqrt{\hbar\omega - E_g} \left(\frac{1}{1 + \exp(\hbar\omega - E_{F,c})/k_B T} - f_{v,0} \right), \end{aligned} \tag{3.3.3}$$

where $(1 - f_v)$ is the hole occupation and $f_{v,0}$ is the electron occupation at the top of the valence band. Note that the optical gain originates from the balance between stimulated emission and absorption, where the absorption generates the minus sign in front of $f_{v,0}$. Our extended model includes four additional fit parameters. The bandgap energy E_g, the Fermi energy $E_{F,c}$, and the effective temperature T can be determined experimentally by comparing the measured spontaneous emission spectrum of the bare sample, depicted in Fig. 3.1b, with the above equation. This leaves only one adjustable parameter, being the valence band occupation $f_{v,0}$ which controls the amount of absorption. We note that the outcome of the model is not very sensitive to the exact value of this parameter and use $f_{v,0} \sim 0.5$ to obtain reasonably good agreement with the experimental data.

3.4 Results

In this section we present measurements of the resonance frequencies of the four SP modes, their widths and total intensities. These measurements are in essence contained in the false-color plots of the measured (angle- and polarization-dependent) spontaneous emission spectra shown in Fig. 3.3a and b. In Fig. 3.3a three p-polarized resonances are visible, labeled with A, B and C. Fig. 3.3b shows one intense s-polarized resonance, labeled S. We analyzed these measurements with two different versions of a coupled-mode model to obtain physical relevant

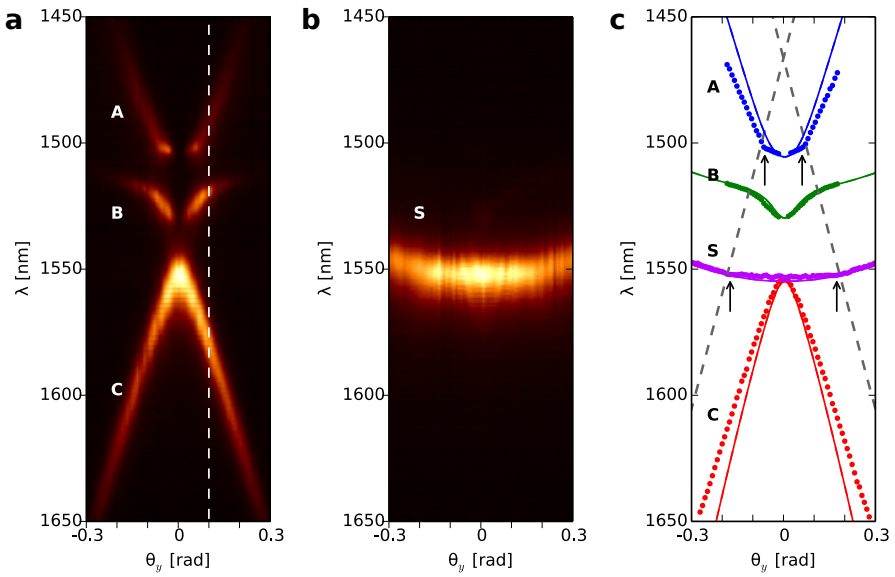

Figure 3.3: False color plots of the measured fluorescence intensity $I(\theta_y, \lambda)$ of a) p-polarization and b) s-polarization. The y-axis depicts energy, in units of vacuum wavelength of the collected photons. The white dashed line in a) at $\theta_y = 0.10$ indicates the cross section shown in Fig. 3.1. c) The resonance frequencies of the bands deduced from the measurements. The dashed lines show the light line of the semiconductor. The arrows mark clear kinks in the dispersion relation.

phenomena and parameters. The two models predict similar dispersion curves, but differ in their predictions of modal linewidths and intensities. Most of the extra parameters required for the advanced model can be obtained for the fluorescence spectrum measured in the absence of gold: the fit curve depicted in Fig. 1b) yields an effective temperature (190K), band filling (down to 1494 nm), and band gap (1653 nm) sample. To remove the unphysical abrupt change at $E = E_{F,c}$ in eq. (3.3.2) and (3.3.3) a convolution with a 17 THz wide Hann window function was used to obtain the spontaneous emission and gain functions used in the advanced model. The subsections below describe the analysis of the resonance frequencies, the widths and the total intensities, respectively.

3.4.1 Resonance frequencies

Figure 3.3c shows the resonance frequencies of all bands. The dispersion of the p-polarized A, B, and C bands shows an avoided crossing. This crossing is

modified by the presence of the (intermediate) B band, which exhibits a remarkable dispersion.

To describe the data we use a coupled mode model, which is described in detail in the appendix. Our measured dispersion curves can be well fitted with amplitude scattering rates $\gamma/\omega_0 = +0.012$ and $\kappa/\omega_0 = \pm 0.004$ and an effective refractive index $n_{eff} = 3.268$ as shown with the solid lines in Fig. 3.3. These values are comparable to values found in ref. [37], where SP dispersion curves measured for nine similar arrays could be well fitted with rates $\gamma/\omega_0 = +0.013$ to $+0.017$ and $\kappa/\omega_0 = \pm 0.005$ to ± 0.011 [37]. We observe that the model deviates from the measured resonance frequencies of the A and C band for larger angles.

Abrupt changes in the dispersion curves of the A and S band are located at $\theta = \pm 0.06$ and $\theta = \pm 0.17$, respectively, and these kinks are marked with arrows in Fig. 3.3c. The A and S band are more flat between the kinks. We do not observe clear kinks in the B and C band. Our relatively simple model does not predict the kinks and flat region of the A and S band. We note that the kinks in the dispersion curves coincide with the positions where they cross the light line of the substrate. This suggests that there is a connection between these kinks and the occurrence of a Rayleigh anomaly, i.e., at the point where an additional diffraction order becomes visible in the substrate. This suggestion is further supported by the observation of a relatively sudden increase in the SP loss rate beyond this point (see below). The dashed light lines in Fig. 3.3c correspond to $n \simeq 3.12$, which is close to the value of $n = 3.10$ of the InP wafer. The thin InGaAs layer and the even thinner SiN_x/InP layer are too thin ($\ll \lambda$) to support a guided (optical) mode and modify this anomaly. We do not yet understand why these kinks are only visible in the S and A band, but not in the B band, which also crosses the light line.

3.4.2 Linewidths

Figure 3.4 shows the observed linewidths of the four SP bands. The C and S band have a large linewidth of $\Delta\omega/\omega \simeq 0.0045$ near $\theta = 0$, while the A and B band have a small linewidth of $\Delta\omega/\omega \simeq 0.001$. The C band is the only band with a linewidth that does not depend on angle. Also the linewidth of the S band is almost constant, except from the sudden increase at $\theta = \pm 0.17$, marked with arrows in Fig. 3.4b. The linewidth of the B band is M shaped, with a minimum at $\theta = 0$.

The basic coupled mode theory, without frequency dependent gain and emission, already explains most of the features that we observe as shown with the dashed lines in Fig. 3.4. For instance, it explains why the SPs in the C and S band are more lossy than the SPs in the A and B band. The reason is that the former scatter efficiently to photons, whereas the latter do not scatter to photons at small angles. At $\theta = 0$ the spectral width of the radiative modes $\Gamma_{C,S} = 2\Gamma_{\mathrm{rad}} + \Gamma_R$ is set by the radiative and reduced ohmic losses, whereas the spectral width of the dark modes $\Gamma_{A,B} = \Gamma_R$ is only determined by the reduced ohmic losses. The experimental results presented in Fig. 3.4 correspond to $\Gamma_R/\omega \leq 0.001$ and $2\Gamma_{\mathrm{rad}}/\omega \simeq 0.004$. This SP-to-photon

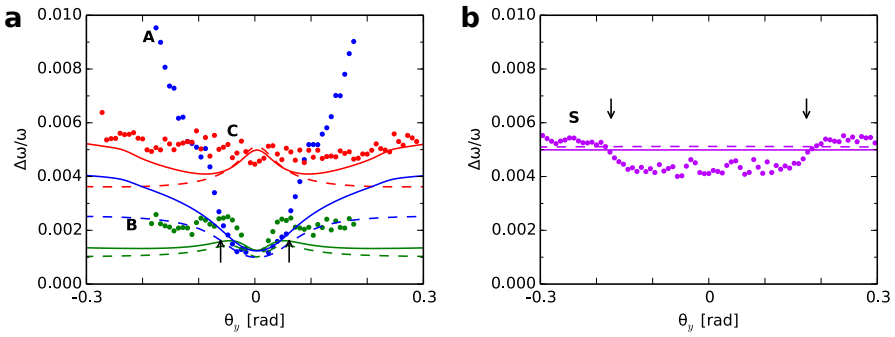

Figure 3.4: Linewidths of the a) p-polarized b) s-polarized bands. The points indicate the experimental values, whereas the curves indicate the predictions of the basic (dashed) and advanced (solid) model. The angle for the observed kink in the A and S band is marked by the arrows.

scattering rate is approximately six times lower than the backscattering rate, but two times higher than the reduced ohmic losses for the applied pump power and temperature.

Extending the model with a frequency dependent gain improves the fits to the A and C band, as shown with the solid lines in Fig. 3.4. Due to the band gap and finite band filling the gain is lower for the A and C band at higher angles. This leads to a larger linewidth at larger angles. The observed linewidth of the A band is still larger than our model predicts. This discrepancy might possibly be explained by both the exact shape of the electron bands in the semiconductor as by a physical description of the Rayleigh anomaly. A good quantitative picture of the Rayleigh anomaly, and in particular the intensity that is carried away by this anomaly is lacking without extensive numerical calculations.

3.4.3 Total intensity

Figure 3.5 shows the integrated intensity, $A = \pi I_{max} \Delta\lambda$, of the individual resonances, where I_{max} is the maximal intensity of the band and $\Delta\lambda$ is its spectral width (half width half maximum). The C and S band have a large integrated intensity with a maximum at $\theta = 0$, whereas the A and B band are much fainter and have a minimum near $\theta = 0$. We call the C and S mode bright/radiative and the A and B mode dark/non-radiative [37].

The first thing to note in Fig. 3.4b is the distinction between the bright C and S bands and the dark A and B bands, in particular around $\theta \approx 0$. This observation is easily understood from the theoretical observation that the bright bands have field maxima at the holes, while the dark bands have field minima at the holes around

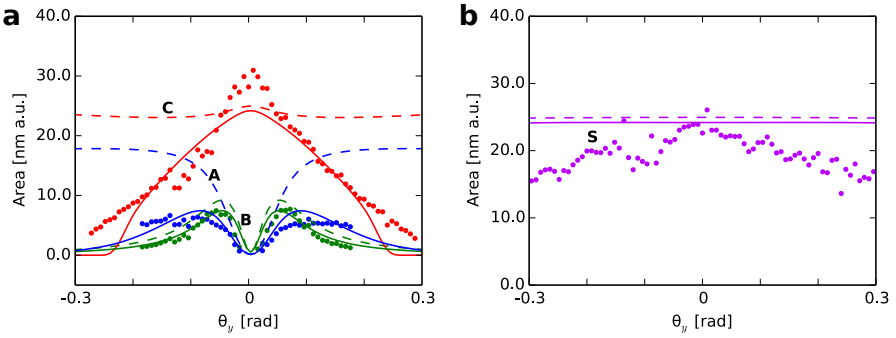

Figure 3.5: Integrated intensity of a) p-polarized and b) s-polarized bands. The points indicate the experimental values, whereas the curves indicate the predictions of the basic (dashed) and advanced (solid) model. Note the large integrated intensity of the bright C and S mode and the small integrated intensity of the dark A and B mode, in particular at $\theta = 0$.

$\theta = 0$. The field we are referring to is the parallel magnetic field, which is the field that scatters SPs to photons [37].

The model without a frequency dependent gain and fluorescence signal reproduces only the main features close to normal incidence, as shown by the dashed lines in Fig. 3.5. It predicts two bright and dark modes, and a M-shaped B band. The fit of the A and C band is improved considerably by including the spectral dependence of the gain and spontaneous emission, as shown with solid lines in Fig. 3.5. In this advanced model, the weak spontaneous emission and gain at short and long wavelengths limit the amount of light in the A and C band at large θ.

3.4.4 Different samples

We repeated these measurements and analyses on different metal hole arrays on the same wafer, with different hole sizes and spacings ($a_0 = 450...470$ nm). All arrays showed similar results, to be more precise: (i) the resonance frequency of the S band showed kinks that occur at the Rayleigh anomaly again, (ii) the spectral width of the two bright modes C and S was larger than that of the two dark modes A and B, and the spectral width of the S band suddenly increased between $\theta_y = 0.1$ and 0.25, and the spectral width of the B band was M-shaped, and (iii) the C and S bands were bright, while the A and B bands were dark at $\theta_y = 0$. There were also differences, one of them was in the width of the A band, which is now constant at small angles, before it increases towards larger angles. The onset of this increase is at the same angle as the kink in the resonance frequency of the A band and coincides with the Rayleigh anomaly.

Furthermore, we studied metal hole arrays with a similar spacing on a different wafer with a thicker (150 nm) active layer. These metal hole arrays did not have a perfect square lattice, but a slightly skewed (2°) parallelogram lattice. The most striking difference with the data presented in Figs 3.3-3.5 was a small bump in the angle dependence of the linewidth of the S band; the measured width of the S is identical to that of the C band at normal incidences, but decreases at $\theta_y = 0.05$. In addition, the resonance frequency of the S band was 4 nm blue-shifted compared to the C band.

3.5 Discussion

To verify that the loss rates and refractive index that are obtained from our model are reasonable, we compared them with theoretical values. The complex refractive index of surface plasmons on a smooth metal-semiconductor interface is

$$n_{eff} + in_i = \sqrt{\frac{\epsilon_1 \epsilon_2}{\epsilon_1 + \epsilon_2}} \tag{3.5.1}$$

where ϵ_1, ϵ_2 are the dielectric constant of the dielectric and the metal respectively. The ohmic loss rate is given by $\Gamma_r/\omega = n_i/n_{eff}$. For transparent InGaAs and InP as dielectric this leads to an expected ohmic loss rate $\Gamma_r/\omega = 0.0053$ and 0.0043 respectively[1]. The very thin SiN_x/InP layer next to the gold interface lowers this value to 0.0033 [20, 62]. Our reduced ohmic loss rate $\Gamma_R/\omega = 0.001$ is lower, which indicates that the InGaAs layer reduces the total loss and hence there is a net gain in the InGaAs layer. However, due to the ohmic losses and SP-to-photon scattering the SP-modes do not have net gain.

In ref. [19], Van Beijnum et al. determined the loss rate of the radiative SP mode around normal incidence, using Fano fits of measured transmission spectra which contained only the radiate modes S and/or C. Their analysis yield a half-width (HWHM) of 12 nm for the resonance around $\lambda = 1562$ nm at low pump power, which narrows to 4 nm at high pump power. The corresponding loss rates are $\Gamma_s/\omega = 0.0077$ and 0.0026, respectively. The loss rate of the unpumped system is considerably larger than our loss rates, while the loss rate of the pumped system is somewhat smaller, which can be explained by the lower temperature used in Ref. [19]. We expect an ohmic loss rate of $\Gamma_R/\omega \approx 0.036$ for the most absorptive case of unpumped bulk InGaAs.

Comparing the basic and advanced model with the data allows us to identify the frequency dependent gain and spontaneous emission as a dominant factor in the system. This frequency dependence depends on the exact shape of the electronic bands in the semiconductor, which might be more complex than our

[1]The following dielectric constants were used for the calculations of the expected loss rates: Gold: $\epsilon = -116 + 11.1i$. Transparent InGaAs: $\epsilon = 11.6$ ($n = 3.407$). InGaAs with absorption (gain):$\epsilon = 11.6 \pm 0.65i$. InP: $\epsilon \approx 9.61$ ($n \approx 3.10$). SiN: $\epsilon \approx 4$ ($n \approx 2$).

simple assumption made in eq. (3.3.2) and (3.3.3). Adding this to the model will increase the complexity and the number of fit parameters, and obscure the relevance of physical phenomena in the model.

3.6 Conclusion

We studied the complex dispersion relation of surface plasmons on a square metal hole array. We observed the frequencies, linewidths, and integrated intensities of the four resonances and compare our data to a simple model designed to identify the key ingredients. This model gives a quantitative prediction for both linewidths and intensities and captures all main features without introducing a large number of unknown parameters. The model necessarily misses some of the observed details. The most notable detail in the experiment are abrupt changes in the resonance frequencies and line widths which coincide with a Rayleigh anomaly.

The basic model is used to deduce the SP-to-photon scattering rate and the reduced ohmic losses. The SP-to-photon scattering rate is found to be approximately six times smaller than the backscattering rate, but is two times higher than the reduces ohmic losses for the applied pump power and temperature. We made a distinction between bright (radiative) and dark (non-radiative) modes. Furthermore we identified the frequency dependent gain as a dominant factor in our model, which should be included in any model of laser action. We augmented the model to include this dominant factor and retrieved improved predictions for both the intensity as the widths of the modes.

Acknowledgement

We acknowledge Frerik van Beijnum, Peter J. van Veldhoven and Erik Jan Geluk for their help in fabricating the samples at the COBRA Research Institute of the Technische Universiteit Eindhoven, The Netherlands.

Appendix

3.A Coupled mode model for SPs in square metal-hole-arrays

3.A.1 SP field in traveling-wave basis

In this appendix we describe a simple coupled-mode model for the surface plasmons (SP) that exist at the metal-dielectric interface of a square hole array. This model is an extension of an earlier model described in ref. [37]. It is based on the notion that photons emitted with parallel momentum $\mathbf{k}_{\parallel} \equiv (k_x, k_y)$ only couple to traveling-wave SPs with (in-plane) momenta $\mathbf{k}_{SP} = \mathbf{k}_{\parallel} + \mathbf{G}_{\mathbf{i}}$, where $\mathbf{G}_i$ is a lattice vector of the hole array. Our model only considers the four dominant Fourier components (modes), with magnitude $|\mathbf{G}_i| \equiv G = (2\pi/a_0)$ pointing in either of the four lattice directions $\{\mathbf{e}_x, \mathbf{e}_{-x}, \mathbf{e}_y, \mathbf{e}_{-y}\}$, and neglects higher-order Fourier components of the SP. These components are not resonant and hardly excited. The

non-resonant contributions from all Fourier components are included in a change in the effective refractive index n_{eff}, which is different from the effective index of SPs on a smooth interface.

In this chapter, we only consider emission at $\theta_x = 0$ and write the parallel momentum $k_y = (\omega/c)\sin\theta_y$ at emission angles $\theta_y \ll 1$. We express the associated out-of-plane components of the SP field at position $\mathbf{r} \equiv (x, y)$ as

$$\begin{aligned}\mathbf{E}(\mathbf{r}, t) = \big[& E_x(t)\mathbf{u}_x e^{iGx} + E_{-x}(t)\mathbf{u}_{-x} e^{-iGx} \\ & + E_y(t)\mathbf{u}_y e^{iGy} + E_{-y}(t)\mathbf{u}_{-y} e^{-iGy} \big] e^{ik_{\parallel} y},\end{aligned} \tag{3.A.1}$$

where $\{E_x, E_{-x}, E_y, E_{-y}\}$ are the modal amplitudes of the four traveling waves. The eigenvectors $\mathbf{u}_i$, which describe the four associated optical polarizations, are chosen to be rotationally-imaged copies of each other. When the four modal amplitudes in Eq. (3.A.1) are combined into a single vector $|E\rangle$, the time evolution of this SP field can be expressed as $d|E\rangle/dt = -iH|E\rangle$, where H is a 4×4 matrix. If scattering is neglected, H reduces to a diagonal matrix with elements $\{\omega_{+x}, \omega_{-x}, \omega_{+y}, \omega_{-y}\}$. At $\theta_x = 0$ and $\theta_y \equiv \theta$, the dispersion relation $\omega = |\mathbf{k}_{\parallel}|c/n_{eff}$ for traveling-wave SPs on a metal-dielectric interface yields $\omega_{\pm y}(\theta) \approx (G \pm k_{\parallel})c/n_{eff} \approx \omega_0 \pm c_1\theta$, and $\omega_x(\theta) = \omega_{-x}(\theta) \approx \omega_0 + c_2\theta^2$, with $\omega_0 \equiv (2\pi/a_0)c/n_{eff}$, $c_1 \equiv \omega_0/n_{eff}$, and $c_2 \equiv \omega_0/(2n_{eff}^2)$, where n_{eff} is the SP effective index.

Reference [37] also described the SP-to-SP scattering processes. This scattering was divided into three fundamental processes: forward scattering under 0° (at a rate γ_0), right-angle scattering under ±90° (at a rate κ), and backwards scattering under 180° (at a rate Γ). Inclusion of these scattering processes into the $d|E\rangle/dt = -iH|E\rangle$ matrix description yields the result presented in ref. [37]:

$$H = \begin{pmatrix} \omega_0 + c_2\theta^2 & \gamma & \kappa & \kappa \\ \gamma & \omega_0 + c_2\theta^2 & \kappa & \kappa \\ \kappa & \kappa & \omega_0 + c_1\theta & \gamma \\ \kappa & \kappa & \gamma & \omega_0 - c_1\theta \end{pmatrix} \tag{3.A.2}$$

The scattering rates γ and κ are assumed to be real-valued, such that the associated coupling is conservative (= energy conserving) and the matrix H is Hermitian. The reference frequency is again $\omega_0 = (2\pi/a_0)c/n_{eff}$, but n_{eff} now contains a small contribution from forward scattering at a rate γ_0.

3.A.2 SP field in standing-wave basis

Next, we transform the evolution matrix H from the traveling-wave to the standing-wave basis. For this purpose, we combine the waves traveling in the $\pm x$ direction into two standing waves with out-of-plane $E_{\perp}(\mathbf{r}) = E_{cx}(\mathbf{r}) \propto \cos Gx \cdot \exp ik_y y$ and $E_{sx}(\mathbf{r}) \propto \sin Gx \cdot \exp ik_y y$, where the labels cx and sx denote a cosine- or sine-pattern in the x direction. Likewise, we combine the $\pm y$ traveling waves into two standing waves with out-of-plane E-fields $E_{cy}(\mathbf{r}) \propto \cos Gy \cdot \exp ik_y y$ and

$E_{sy}(\mathbf{r}) \propto \sin Gy \cdot \exp ik_y y$. The transition from the $\{+x, -x, +y, -y\}$ traveling-wave basis to the $\{-i\sin Gx, \cos Gx, -i\sin Gy, \cos Gy,\}$ or $\{sx, cx, sy, cy\}$ standing-wave basis transforms the H matrix into

$$H = \begin{pmatrix} \omega_0 + c_2\theta^2 - \gamma & 0 & 0 & 0 \\ 0 & \omega_0 + c_2\theta^2 + \gamma & 0 & 2\kappa \\ 0 & 0 & \omega_0 - \gamma & \delta \\ 0 & 2\kappa & \delta & \omega_0 + \gamma \end{pmatrix}, \tag{3.A.3}$$

where $\delta \equiv -c_1\theta = -(\omega_0/n_{eff})\theta$.

Note how the 4×4 matrix separates in an uncoupled element, associated with the sx standing wave, and a 3×3 matrix. This separation results from the mirror symmetry in the xz-plane ($\theta_x = 0$). The $E_{sx}(\mathbf{r}) \propto \sin Gx \cdot \exp ik_y y$ field is the only standing wave that is odd under mirror inversion, while the other three standing waves are even. The former couples only to s-polarized emission, which has an odd symmetry, while the latter three mix and couple to p-polarized emission, which also has an even symmetry. Also note how the coupling rate κ, associated with SP-SP scattering under 90°, only couples the $\cos Gx$ and $\cos Gy$ waves, which have intensity maxima at the holes, while the detuning δ only couples the cy and sy standing waves.

3.A.3 Losses and gain

Next, we include losses and gain in our model. First of all, we include ohmic losses at an ohmic damping rate $\Gamma_r = (n_i/n_{eff})\omega$, where n_i and n_{eff} are the imaginary and real part of the SP effective index $n_{eff} + in_i = \sqrt{\epsilon_1\epsilon_2/(\epsilon_1 + \epsilon_2)}$ at the interface between medium 1 and 2. Second, we include optical gain at a gain rate g_0 per second. As both ohmic loss and optical gain are distributed approximately uniformly, they can be combined into an effective ohmic loss rate $\Gamma_R \equiv \Gamma_r - g_0$ and are easily incorporated in our matrix description by replacing the evolution matrix $iH \rightarrow iH - \Gamma_R$. Finally, we include radiative losses through scattering from SPs to photons, either in the air or in the semiconductor. This radiative loss rate $\Gamma_{\text{rad}} = \Gamma_{air} + \Gamma_{semi}$ is equal for all traveling waves, but mode selective for the standing waves. As radiative scattering only occurs at the holes and as the SP-to-photon coupling proceeds dominantly via the in-plane magnetic field (at $\theta \ll 1$), we expect that only the standing waves with a sinusoidal $E_\perp$- pattern couple radiatively, at a decay rate $2\Gamma_{\text{rad}}$, while the cosine-type modes don't couple. By combining the above loss and gain rate into our matrix description we arrive at our final expression

$$H = \begin{pmatrix} \tilde{\omega}_{sx} & 0 & 0 & 0 \\ 0 & \tilde{\omega}_{cx} & 0 & 2\kappa \\ 0 & 0 & \tilde{\omega}_{sy} & \delta \\ 0 & 2\kappa & \delta & \tilde{\omega}_{cy} \end{pmatrix}, \tag{3.A.4}$$

where $\tilde{\omega}_i = \omega_i - i\Gamma_i$ are four complex frequencies, with real parts $\omega_{sx} = \omega_0 + c_2\theta^2 - \gamma$, $\omega_{cx} = \omega_0 + c_2\theta^2 + \gamma$, $\omega_{sy} = \omega_0 - \gamma$, and $\omega_{cy} = \omega_0 + \gamma$, and imaginary parts $\Gamma_{sx} = \Gamma_{sy} = \Gamma_R + 2\Gamma_{\text{rad}}$ and $\Gamma_{cx} = \Gamma_{cy} = \Gamma_R$.

3.A.4 Spontaneous emission spectra

The fluorescence spectrum of the optically-pumped systems can be calculated in two steps, once the evolution matrix of the SP-field is known. In the first step, the spontaneous emission into the surface plasmon manifold is calculated from the expression

$$\frac{d}{dt}|E(t)\rangle = -iH|E(t)\rangle + |S(t)\rangle \quad \Rightarrow \quad |E(\omega)\rangle = -i(H-\omega)^{-1}|S(\omega)\rangle ,$$

where the 4-element vector $|S\rangle$ describes the original spontaneous emission, divided over the four standing-wave SP modes, and $|E\rangle$ describes the generated SP field. The multiplication by $(H-\omega)^{-1}$ describes how the original emission source is modified by the gain and loss in the system into the resulting SP field, which therefore peaks around optical frequencies ω close to the complex poles of the matrix H. In the first step of the calculation, we assume that the original emission at each optical frequency is equally distributed over the four standing waves and that the four emitted fields are uncorrelated. This assumption is the Fourier equivalent of the statement that the original emission at different spatial positions is homogeneous, isotropic, and uncorrelated. The emitters are thus treated as classical noise sources with a strength that depends only on their excited-state and ground-state population, as was done in the analysis of spontaneous emission noise in semiconductor lasers [63]. In the second (and final) step, the generated surface plasmons are scattered into photons and detected. The sx standing SP wave scatters into s-polarized photons and only the sy standing SP wave is assumed to scatter into p-polarized photons.

The emission in the (odd) s-polarized mode is easily calculated. As only one of the four SP standing waves is odd, the SP field follows from the scalar relation $E(\omega) = iS(\omega)/(\omega - \tilde{\omega}_{sx})$ and its absolute square

$$I_{\text{s-polarization}}(\omega) \propto \frac{I_s(\omega)}{(\omega-\omega_{sx})^2 + \Gamma_{sx}^2} , \tag{3.A.5}$$

where $I_s(\omega) \longleftrightarrow |S(\omega)|^2$. We recognize the standard Lorentzian form, with its resonance frequency $\omega_{sx} \equiv \omega_0 + c\delta^2 - \gamma$ and its (HWHM) half-width $\Gamma_{sx} \equiv \Gamma_R + 2\Gamma_{\text{rad}}$. The excited sx mode emits efficiently from SP-to-photon, as this $E_{sx}(\mathbf{r}) \propto \sin Gx \cdot \exp ik_y y$ mode has a magnetic field $\mathbf{H}_{sx}(\mathbf{r}) \propto \cos Gx \cdot \exp ik_y y \mathbf{e}_y$ with anti-nodes at the holes.

A calculation of the (even) p-polarized emission is more complicated, as this emission originates from three coupled SP modes. After some straightforward

mathematics, which involves the inversion of a 3×3 matrix and a projection onto the sy mode, which is the only one of the three mode that couples to photons, we obtain

$$I_{\text{p-polarization}}(\omega) \propto \sum_{i=1}^{3} \frac{I_s(\omega)\,|\langle sy|u_i\rangle|^2}{(\omega-\omega_i)^2+\Gamma_i^2} \tag{3.A.6}$$

where $\langle u_i|$ are the three left eigenvectors of the 3×3 lower-right submatrix $\tilde{H}$ of H, $\tilde{\omega}_i \equiv \omega_i + i\Gamma_i$ are the associated eigenvalues, such that $\langle u_i|\tilde{H} = \tilde{\omega}_i\langle u_i|$, and $|sy\rangle$ denotes the field of the sy mode. The explicit solution of this problem reads

$$I_{\text{p-polarization}}(\omega) \propto \frac{\left|\left(\tilde{\omega}_{cy}-\omega\right)(\tilde{\omega}_{cx}-\omega)-4\kappa^2\right|^2+\delta^2\left[|\tilde{\omega}_{cx}-\omega|^2+4\kappa^2\right]}{\left|\left(\tilde{\omega}_{sy}-\omega\right)\left[\left(\tilde{\omega}_{cy}-\omega\right)(\tilde{\omega}_{cx}-\omega)-4\kappa^2\right]-\delta^2(\tilde{\omega}_{cx}-\omega)\right|^2} I_s(\omega), \tag{3.A.7}$$

At $\delta = 0$ and $\kappa = 0$, we recover the expected result $I_{\text{p-polarization}}(\omega) = I_{\text{s-polarization}}(\omega) \propto I_s(\omega)/|\tilde{\omega}_{sy}-\omega|^2$.

The above expressions for the emitted spectrum contain subtleties that might go unnoticed in their present form, as they are related to the frequency dependence of some of its parameters. The spontaneous emission spectrum $I_s(\omega)$ and the associated stimulated emission or optical gain $g(\omega)$ will for instance depend on frequency. These effects are included in the advanced model used in the main text. To keep the description simple, and limited the number of fit parameters, we have not yet included the following two effects: (i) The SP-to-SP scattering rates γ and κ and the SP-to-photon scattering rate Γ_{rad} are expected to show a wavelength dependence, with Rayleigh-type scattering rates scaling as ω^n with $n \geq 6$, depending on the type of scattering [64], (ii) the appearance of a new diffraction order (Rayleigh anomaly) is expected to lead to a sudden increase in radiative loss at large angle.